

# Structure and properties of TiN(111)/Si<sub>x</sub>N<sub>y</sub>/TiN(111) interfaces in superhard nanocomposites: First-principles investigations

Shiqiang Hao,<sup>1</sup> Bernard Delley,<sup>2</sup> and Catherine Stampfl<sup>1,\*</sup><sup>1</sup>*School of Physics, The University of Sydney, Sydney NSW 2006, Australia*<sup>2</sup>*Paul Scherrer Institut, WHGA/123, CH-5232 Villigen PSI, Switzerland*

(Received 25 September 2005; published 6 July 2006)

We perform first-principles calculations based on density-functional theory to investigate the role of interfaces in superhard nanocomposites. A prerequisite is clearly knowledge of the detailed atomic structure, which is addressed in the present paper. In particular, we study the relative stability of TiN(111)/Si<sub>x</sub>N<sub>y</sub>/TiN(111) interfaces, which form in the highly thermally stable *nc*-TiN/*a*-Si<sub>x</sub>N<sub>y</sub> nanocomposites. For nitrogen-rich conditions, the most favorable configurations involve very thin layers of Si, which are purely nitrogen coordinated and tetrahedrally bonded. For increasingly nitrogen-poor conditions, interfaces involving Ti-Si-N, and predominantly octahedral Ti-Si-Ti, bonding are preferred. The atomic geometry and associated electronic structure are discussed for these interfaces, as well as properties of the bulk  $\alpha$ ,  $\beta$ , and  $\gamma$  phases of Si<sub>3</sub>N<sub>4</sub>, TiN, and TiSi<sub>2</sub>.

DOI: [10.1103/PhysRevB.74.035402](https://doi.org/10.1103/PhysRevB.74.035402)

PACS number(s): 81.05.Je, 68.35.Dv, 73.22.-f

## I. INTRODUCTION

Titanium nitride is an important early transition metal nitride known for its extreme and desirable physical properties of hardness, high-melting point, and high resistance to corrosion.<sup>1,2</sup> The exceptional hardness affords the use of TiN as a high-performance coating material for cutting tools. Similarly, owing to its outstanding mechanical properties, silicon nitride plays a prominent role as a ceramic with high strength, hardness, and resistance to corrosion, and has found industrial applications as a high-temperature-resistant material.<sup>3</sup> In addition, it is an important material in microelectronics due to its high resistivity, higher dielectric constant compared to silicon dioxide, and as mentioned above, mechanical strength and chemical inertness.<sup>4</sup> Recently, a new concept for the design of novel superhard coatings has combined these two compounds.<sup>5</sup> The approach apparently exploits the natural formation, through spinodal decomposition, of an strong interface between titanium nitride nanocrystallites (*nc*) and amorphous (*a*) silicon nitride regions. The interfaces are thought to prevent grain boundary sliding and dislocation propagation and, thus, contribute to the found significant enhancement in the hardness as compared to the pure constituents. The nanocomposite, so-called *nc*-TiN/*a*-Si<sub>3</sub>N<sub>4</sub>, is reported to exhibit a hardness maximum when prepared with only a very thin film of silicon nitride (0.3–0.5 nm) between the TiN nanocrystallites, which are of the order of 3–4 nm.<sup>5</sup> In particular, the reported Vicker's hardness<sup>5</sup> of 50 GPa is significantly higher than that of TiN (18 GPa) or Si<sub>3</sub>N<sub>4</sub> (33 GPa,  $\gamma$  phase; 30 GPa,  $\beta$  phase<sup>6</sup>) alone.<sup>7</sup> On this basis, a series of ternary and quaternary superhard nanocomposites have been prepared, e.g., *nc*-TiN/*a*-BN and *nc*-TiN/*a*-TiB<sub>x</sub>/*a*-BN with reported hardnesses in the range of 45–50 GPa,<sup>8</sup> while the hardness of *nc*-TiN/*a*-Si<sub>3</sub>N<sub>4</sub>/*a*- and *nc*-TiSi<sub>2</sub> was reported to reach 80–105 GPa.<sup>9</sup> Importantly, the superhard nanocomposite coatings, consisting of a transition metal nitride and a non-metallic nitride, remain stable in terms of their nanostructure and superhardness up to temperatures exceeding 1100 °C.<sup>10</sup>

This is in contrast to other superhard films prepared using energetic ion bombardment or epitaxial stabilization of metastable multilayers, which often exhibit a loss in hardness at considerably lower temperatures.<sup>11</sup>

Recently, there has been some controversy regarding the reported hardnesses of these above-mentioned nanocomposite systems, where there has been some difficulty reproducing the values quoted above.<sup>12</sup> The reason for this has been attributed to either oxygen contamination and/or because a too low temperature or a too low nitrogen pressure was used during the deposition,<sup>13,14</sup> which prevents the formation of the “correct” interface structure. The significant hardness enhancement of the nanocomposite *nc*-TiN/*a*-Si<sub>3</sub>N<sub>4</sub> is supported by recent studies of nanostructured multilayer films consisting of TiN and SiN<sub>x</sub>. In particular, Söderberg *et al.*<sup>15</sup> reported a maximum hardness enhancement of about 33 GPa when the thickness of the SiN<sub>x</sub> interlayer was 0.3 nm and the TiN thickness 4.5 nm. Also, Chen *et al.*<sup>16</sup> reported a hardness of in excess of 45 GPa for a TiN layer thickness of 2.0 nm and a SiN<sub>x</sub> thickness of 0.5 nm. A similar trend has been reported by Hu *et al.*<sup>17</sup> In these three studies, it was reported that the SiN<sub>x</sub> interface structure forms epitaxially on TiN.

In order to gain insight into understanding the reason for the hardness enhancement in such nanocomposites, it is necessary to first have knowledge of the atomic structure of the interface between the nanocrystalline and amorphous structures. It is the aim of the present paper to investigate this aspect for the *nc*-TiN/*a*-Si<sub>3</sub>N<sub>4</sub> system, as well as to determine the associated physical and electronic properties through density-functional theory (DFT) calculations.

Quantitative experimental information concerning the interfaces of *nc*-TiN/*a*-Si<sub>3</sub>N<sub>4</sub> nanocomposites include high-resolution transmission electron microscopy (HRTEM) studies,<sup>18</sup> which show that the main crystallographic orientation relationship is [0001] Si<sub>3</sub>N<sub>4</sub> || [110] TiN with (10 $\bar{1}$ 0) Si<sub>3</sub>N<sub>4</sub> || (1 $\bar{1}$ 1) TiN. Also, x-ray photoelectron spectroscopy (XPS) results<sup>9</sup> indicate that the Si atoms in *nc*-TiN/*a*-Si<sub>3</sub>N<sub>4</sub> nanocomposites are bonded only to N atoms, on the basis that the binding energy of the Si-2*p* state corre-

sponds very closely to that which it has in bulk  $\beta$ - $\text{Si}_3\text{N}_4$ . The  $\{111\}$  lattice planes of TiN are polar, terminated by either nitrogen or titanium atoms; similarly, the  $\{10\bar{1}0\}$  lattice planes of  $\alpha$ - and  $\beta$ - $\text{Si}_3\text{N}_4$  are polar containing either nitrogen or silicon atoms. Therefore, in the interface, it is conceivable that nitrogen atoms are shared between silicon nitride and titanium nitride.

The outline of the paper is as follows. In Sec. II we explain our calculation method and in Sec. III the bulk properties of TiN,  $\text{TiSi}_2$ , and  $\alpha$ -,  $\beta$ -, and  $\gamma$ - $\text{Si}_3\text{N}_4$  are described. The atomic geometry, formation energy, and electronic structure of the interface structures are presented in Sec. IV, and the conclusion is given in Sec. V.

## II. CALCULATION METHOD

All the DFT calculations are performed using the DMol<sup>3</sup> program<sup>19,20</sup> with the generalized gradient approximation (GGA)<sup>21</sup> for the exchange-correlation functional. In DMol<sup>3</sup>, the wave functions are expanded in terms of accurate numerical basis-sets. We use the double-numeric quality basis-set with polarization functions (DNP) and pseudopotentials, which include scalar relativistic corrections (VPSR). Convergence tests show that an atomic cutoff radius of 9 Bohr is sufficient (see below). The particular  $\mathbf{k}$ -point sampling and supercells employed are described for the individual systems below.

To determine the equilibrium structure of bulk silicon nitride, titanium nitride, and titanium disilicide, we use the Murnaghan equation of state.<sup>22</sup> For the bulk  $\alpha$ -,  $\beta$ -, and  $\gamma$ - $\text{Si}_3\text{N}_4$  phases, we fully optimize the internal coordinates of the atoms to minimize the total energy. For the TiN(111)/ $\text{Si}_x\text{N}_y$ /TiN(111) interface structures described in Section IV A, all atoms are allowed to move without any constraints. After relaxation, the remaining forces on the atoms are  $<0.01$  eV/Å.

The heat of formation of the bulk materials ( $\alpha$ -,  $\beta$ -,  $\gamma$ - $\text{Si}_3\text{N}_4$ , TiN, and  $\text{TiSi}_2$ ) is calculated as

$$\Delta H_f = E_{\text{tot}} - \sum_i n_i E_i, \quad (1)$$

where  $E_{\text{tot}}$  is the total energy of the bulk phase with  $n_i$  atoms of species  $i$ , and  $E_i$  is the total energy of a bulk Si or Ti atom, or half the energy of an  $\text{N}_2$  molecule for  $i=\text{Si}, \text{Ti}$  and  $\text{N}$ , respectively. For calculating the total energy (including spin-polarization) of  $\text{N}_2$  and the free Si atom (as required below in evaluating the adsorption energy), we use the molecular DMol code.

The surface energy  $\sigma$  is calculated as

$$\sigma = 1/2 \left( E_{\text{tot}}^{\text{slab}} - \sum_j n_j E_j \right), \quad (2)$$

where  $E_{\text{tot}}^{\text{slab}}$  is the total energy of the slab used to model the surface, and  $n_j$  and  $E_j$  are the number of units of TiN in the slab, and the corresponding total energy, respectively. For a polar surface, the surface energy will be the average of the two differently terminated surfaces of the slab.

The interfacial formation energy  $E^f$  is an important quantity that is affected by local chemical bonding and strain

effects due to lattice mismatch. To evaluate the relative stabilities of the various interface structures, we calculate  $E^f$  as

$$E^f(\mu_{\text{Si}}, \mu_{\text{N}}, \mu_{\text{Ti}}) = \frac{(E_{\text{tot}}^{\text{int}} - E_{\text{slab}}^{\text{TiN}} - n\mu_{\text{N}} - m\mu_{\text{Si}} - l\mu_{\text{Ti}})}{S}, \quad (3)$$

where  $E_{\text{tot}}^{\text{int}}$  and  $E_{\text{slab}}^{\text{TiN}}$  are the total energies of the interfacial system under consideration and a 20-layer TiN(111) slab with interface area  $S$ ;  $\mu_{\text{N}}$ ,  $\mu_{\text{Si}}$  and  $\mu_{\text{Ti}}$  are the nitrogen, silicon, and titanium atom chemical potentials, and  $n$ ,  $m$ , and  $l$  are the number of N, Si, or Ti atoms that are added to the TiN slab in order to create the interface of interest. The interface [i.e., the  $\text{Si}_x\text{N}_y$  (or SiTi) layer(s)] is located in the center of the 20-layer TiN(111) slab, which is surrounded by a vacuum region of 20 Å. Here “one layer” means a pure N or Ti layer, not a “double” (TiN) layer; thus, there are 20 atoms in the “(1 × 1) 20-layer TiN(111) slab.”

To help make contact with experimental conditions, we consider  $E^f$  for so-called nitrogen-rich and nitrogen-poor (or Ti-rich) conditions. For the former, it means in Eq. (3) we use  $\mu_{\text{N}} = \frac{1}{2}E_{\text{N}_2}$  (half the total energy of the  $\text{N}_2$  molecule) and for the latter we use  $\mu_{\text{Ti}} = E_{\text{Ti}}^{\text{bulk}}$ , which is the total energy of a bulk hcp Ti atom. We assume that in equilibrium,  $\mu_{\text{TiN}} = \mu_{\text{Ti}} + \mu_{\text{N}}$ , where  $\mu_{\text{TiN}}$  is the chemical potential of bulk rock-salt TiN. For N-rich conditions, we then have  $\mu_{\text{Ti}} = E_{\text{TiN}} - \frac{1}{2}E_{\text{N}_2}$ , and similarly, for N-poor conditions we have  $\mu_{\text{N}} = E_{\text{TiN}} - E_{\text{Ti}}^{\text{bulk}}$ . For the Si atom chemical potential,  $\mu_{\text{Si}}$ , under nitrogen-rich conditions, we assume an upper limit determined by bulk  $\beta$ - $\text{Si}_3\text{N}_4$ , that is  $\mu_{\text{Si}_3\text{N}_4} = 3\mu_{\text{Si}} + 4\mu_{\text{N}}$ , where  $\mu_{\text{Si}_3\text{N}_4}$  is the chemical potential of bulk  $\beta$ - $\text{Si}_3\text{N}_4$ . Then we have  $\mu_{\text{Si}} = \frac{1}{3}(E_{\text{tot}}^{\text{Si}_3\text{N}_4} - 2E_{\text{tot}}^{\text{N}_2})$ , where  $E_{\text{tot}}^{\text{Si}_3\text{N}_4}$  is the total energy of a bulk unit of  $\beta$ - $\text{Si}_3\text{N}_4$ . For N-poor conditions, we assume an upper limit of the Si chemical potential determined by bulk  $\text{TiSi}_2$ , that is  $\mu_{\text{TiSi}_2} = \mu_{\text{Ti}} + 2\mu_{\text{Si}}$ , where  $\mu_{\text{TiSi}_2}$  is the chemical potential of bulk  $\text{TiSi}_2$ . Then we have  $\mu_{\text{Si}} = \frac{1}{2}(E_{\text{tot}}^{\text{TiSi}_2} - E_{\text{Ti}}^{\text{bulk}})$  where  $E_{\text{tot}}^{\text{TiSi}_2}$  is the total energy of a bulk unit of  $\text{TiSi}_2$ . This is explained in more detail in Sec. IV B.

## III. BULK PROPERTIES

### A. $\alpha$ -, $\beta$ -, and $\gamma$ - $\text{Si}_3\text{N}_4$

There are four kinds of experimentally reported crystalline  $\text{Si}_3\text{N}_4$  phases that have relatively complex atomic configurations. The structure of the  $\alpha$  phase, with space group P31c, is a trigonal system containing 28 atoms per unit cell with the  $c$  axis about twice that of the  $\beta$  phase. All N atoms lie out of the plane of their three Si neighbors, and all Si atoms are fourfold coordinated to nitrogen. The structure of  $\beta$ - $\text{Si}_3\text{N}_4$  is hexagonal with 14 atoms per unit cell with P6<sub>3</sub>/m symmetry.<sup>23</sup> In this structure, all Si atoms surrounded by nitrogen are fourfold coordinated at the center of a distorted tetrahedron, which is the  $6h$  site. While all nitrogen atoms are threefold coordinated, the nitrogen atoms in the  $2c$  site are in a planar geometry with respect to the three nearest silicon atoms, and the nitrogen atoms in the  $6h$  site lie out of the plane of the nearest Si atoms. Another  $\beta$  phase, without mirror symmetry in the space group of P6<sub>3</sub>, has also been experimentally reported.<sup>24</sup> Investigations of the relative sta-

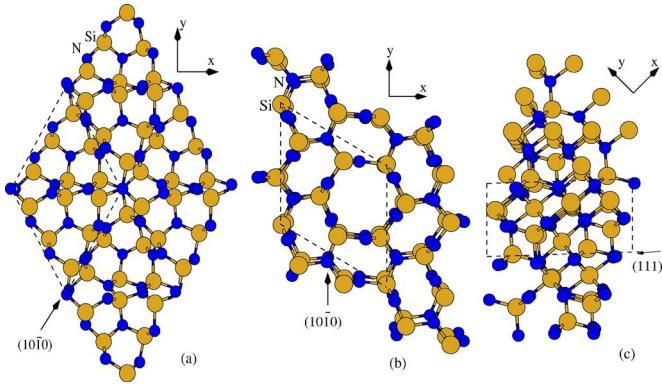


FIG. 1. (Color online) Atomic structure of (a)  $\alpha$ - $\text{Si}_3\text{N}_4$  (P31c), (b)  $\beta$ - $\text{Si}_3\text{N}_4$  (P6<sub>3</sub>/m), and (c)  $\gamma$ - $\text{Si}_3\text{N}_4$  (Fd $\bar{3}$ m). The dashed lines indicate the unit cells. Various atomic planes are indicated by the arrows, where the planes lie parallel to the direction of the arrows, and are perpendicular to page. (The  $z$  direction is perpendicular to the page.) Large gray and small black circles represent Si and N atoms, respectively.

bility of the two kinds of  $\beta$  phases using the pseudopotential plane-wave method<sup>25</sup> suggest an opposite conclusion to what was derived by the orthogonalized linear combination of atomic orbitals (OLCAO) method,<sup>26</sup> and show that the P6<sub>3</sub>/m structure is naturally recovered through relaxation from the P6<sub>3</sub> initial configuration. In fact, the structures of these two  $\beta$  phases are quite similar with only slight differences in the  $z$  coordinates of the N atoms. In the present work, we only consider the P6<sub>3</sub>/m phase. The structure of the  $\gamma$  phase of  $\text{Si}_3\text{N}_4$  is isomorphic to the mineral spinel  $\text{MgAl}_2\text{O}_4$  with 14 atoms in the unit cell.<sup>27,28</sup> It is cubic with space group Fd $\bar{3}$ m. The Si atoms in the  $8a$  site are tetrahedrally bonded to N atoms, and the remaining Si atoms in the  $16d$  sites are octahedrally coordinated to six nitrogen atoms. All nitrogen atoms are equivalent in the  $32e$  site with one Si neighbor in the  $8a$  site and the other three Si neighbors residing in the  $16d$  site. The atomic geometry of all three structures are shown in Fig. 1.

In calculating the equilibrium atomic structures of  $\alpha$ -,  $\beta$ -, and  $\gamma$ - $\text{Si}_3\text{N}_4$ , we use Monkhorst-Pack<sup>33</sup> meshes of  $(2 \times 2 \times 4)$ ,  $(2 \times 2 \times 6)$ , and  $(4 \times 4 \times 4)$ , yielding 6, 8, and 8  $\mathbf{k}$ -points in the irreducible part of the Brillouin zone (IBZ), respectively. Increasing the mesh for  $\beta$ - $\text{Si}_3\text{N}_4$  to  $(4 \times 4 \times 6)$  (12  $\mathbf{k}$ -points in the IBZ), changes the total energy by only 0.0013 eV per atom. We use a cutoff radius of 9 Bohr for all three bulk phases. Increasing this to 10 Bohr for the  $\beta$ - $\text{Si}_3\text{N}_4$  phase changes the total energy by only 0.001 eV per atom and alters the equilibrium lattice constant by only 0.005 Å. Similar small changes are found for increasing the number of  $\mathbf{k}$ -points and cutoff radii for the other two phases. The calculated atomic structure and bulk moduli of the three  $\text{Si}_3\text{N}_4$  phases are listed in Table I, where we compare to experimental results and to other *ab initio* calculations. It can be seen that there is excellent agreement of the lattice constants of the three phases with experiment, with the largest deviation being 0.5% for the  $\beta$  phase. From fitting the total energy vs volume curve to the Murnaghan equation of state as shown in Fig. 2, we obtain the bulk moduli of 242, 273,

and 304 GPa for the  $\alpha$ ,  $\beta$ , and  $\gamma$  phases, respectively. The results for the bulk moduli are in very good agreement with available experimental and theoretical results. The heat of formation of the three  $\text{Si}_3\text{N}_4$  phases are calculated to be  $-7.794$ ,  $-7.814$ , and  $-7.158$  eV per  $\text{Si}_3\text{N}_4$  unit for the  $\alpha$ ,  $\beta$ , and  $\gamma$  phases, respectively. They are very close to the experimental value of  $-7.702$  eV per  $\alpha$ - $\text{Si}_3\text{N}_4$  unit as reported in Ref. 34, but somewhat lower than the experimental values of  $-8.60 \pm 0.04$  eV and  $-8.58 \pm 0.03$  eV for the  $\alpha$  and  $\beta$  phases, as reported in Ref. 35. Other experimental values in the literature apparently range from  $-6.44 \pm 0.83$  eV to  $-8.73 \pm 0.03$  eV and the difference between the  $\alpha$  and  $\beta$  phases vary from negligible to 0.31 eV.<sup>36</sup> Thus, there is some uncertainty regarding the precise experimental values. Our calculations find the  $\alpha$  phase slightly higher in energy than the  $\beta$  phase, but by only 0.02 eV per formula unit. Since the structure and bonding are very similar in the  $\alpha$  and  $\beta$  phases, the small difference is not surprising. The corresponding value of 0.217 eV per formula unit, as reported by the OLCAO calculations,<sup>26</sup> is notably larger than our results. The  $\gamma$  phase is calculated to be considerably higher in energy than the  $\alpha$  or  $\beta$  phases, by nearly 0.66 eV per formula unit, can be compared to the value of  $\sim 1$  eV as obtained from the first-principles calculations reported in Ref. 27.

## B. Rocksalt TiN

For calculation of the physical properties of bulk rock-salt TiN we use a cutoff radius of 9 Bohr and a Monkhorst-Pack  $\mathbf{k}$ -point mesh of  $(8 \times 8 \times 8)$ , yielding 29  $\mathbf{k}$  points in the IBZ. We obtain a lattice constant of 4.259 Å, which is very close to the experimental result of 4.24 Å<sup>44</sup> and to the result obtained by the full-potential linear augmented plane wave (FLAPW) method of 4.26 Å.<sup>45</sup> Increasing the cutoff radius to 10 Bohr changes the total energy by only 0.007 eV per atom, and the equilibrium lattice constant by 0.004 Å. With a finer  $\mathbf{k}$ -point mesh of  $(9 \times 9 \times 9)$  (producing 35  $\mathbf{k}$  points in the IBZ), the total energy changes by only 0.017 eV. The heat of formation is calculated to be 3.43 eV per TiN unit, which is very close to the experimentally reported value of 3.46 eV,<sup>34</sup> and to the FLAPW-GGA result of 3.56 eV.<sup>45</sup>

We also calculate the surface energy of the low-index TiN surfaces, namely, (111), (100), and (110), where we used 8, 9, and 8 layers, respectively. The  $\mathbf{k}$ -point sampling was carried out using Monkhorst-Pack meshes of  $(6 \times 6 \times 1)$  (11  $\mathbf{k}$  points in the IBZ),  $(6 \times 6 \times 1)$  (10  $\mathbf{k}$  points in the IBZ), and  $(8 \times 8 \times 1)$  (21  $\mathbf{k}$  points in the IBZ), respectively for the (111), (100), and (110) surfaces. We found that when increasing the number of layers from 8 to 10 for TiN(111), the surface energy of the unrelaxed and relaxed TiN(111) surfaces changed by only  $6 \times 10^{-5}$  eV/Å<sup>2</sup> and  $4 \times 10^{-4}$  eV/Å<sup>2</sup>, respectively. For the (110) surface, increasing the slab thickness from 8 to 10 layers changed the relaxed surface energy by only 0.001 eV/Å<sup>2</sup>. The surface energies are listed in Table II, where we compare to other DFT-GGA results. As can be seen, the greatest deviation occurs for the (111) surface where the values reported in Ref. 47 are notably higher than those of Ref. 46 and the present work. The (100) surface

TABLE I. Lattice constants,  $a$  and  $c$ , atomic positions relative to the magnitude of the unit cell vectors, and bulk moduli,  $B_0$ , for the  $\alpha$ -,  $\beta$ -, and  $\gamma$ - $\text{Si}_3\text{N}_4$  phases as obtained in the present work, from experiment, and by other *ab initio* calculations.

$\alpha$	This work	Experiment	Other <i>ab initio</i> calculations
$a$ (Å)	7.804	7.766 <sup>a</sup>	7.792 <sup>b</sup>
$c$ (Å)	5.649	5.615 <sup>a</sup>	5.614 <sup>b</sup>
Si <sub>1</sub> (6c)	0.5118, 0.4291, 0.660	0.5130, 0.4305, 0.6580 <sup>a</sup>	0.511, 0.4283, 0.6542 <sup>b</sup>
Si <sub>2</sub> (6c)	0.1675, 0.9139, 0.4532	0.168, 0.915, 0.4504 <sup>a</sup>	0.1634, 0.9123, 0.4513 <sup>b</sup>
N <sub>1</sub> (6c)	0.6104, 0.9545, 0.4333	0.6124, 0.9592, 0.4343 <sup>a</sup>	0.6149, 0.9621, 0.4387 <sup>b</sup>
N <sub>2</sub> (6c)	0.3197, 0.00545, 0.7014	0.3199, 0.0046, 0.7045 <sup>a</sup>	0.3264, 0.0262, 0.6903 <sup>b</sup>
N <sub>3</sub> (2a)	0.0, 0.0, 0.4538	-, -, 0.4520 <sup>a</sup>	-, -, 0.4312 <sup>b</sup>
N <sub>4</sub> (2b)	1/3, 2/3, 0.1047	-, -, 0.1015 <sup>a</sup>	-, -, 0.1398 <sup>b</sup>
$B_0$ (GPa)	242	228 <sup>c</sup> ; 248 <sup>d</sup>	257 <sup>b</sup> ; 227 <sup>e</sup>
$\beta$			
$a$ (Å)	7.652	7.607 <sup>f</sup>	7.622 <sup>b</sup> ; 7.562 <sup>g</sup> ; 7.61 <sup>h</sup>
$c$ (Å)	2.927	2.911 <sup>f</sup>	2.910 <sup>b</sup> ; 2.893 <sup>g</sup> ; 2.91 <sup>h</sup>
Si (6h)	0.1738, 0.7678, 0.25	0.174, 0.766, - <sup>f</sup>	0.1723, 0.7645, - <sup>b</sup> ; 0.1741, 0.7677, 0.25 <sup>g</sup>
N <sub>1</sub> (2c)	1/3, 2/3, 0.25		
N <sub>2</sub> (6h)	0.329, 0.030, 0.25	0.321, 0.025, - <sup>f</sup>	0.3341, 0.025 - <sup>b</sup> ; 0.3302, 0.0298, 0.25 <sup>g</sup>
$B_0$ (GPa)	273	258 <sup>i</sup> ; 273 <sup>j</sup>	274 <sup>b</sup> ; 249 <sup>e</sup>
$\gamma$			
$a$ (Å)	7.783	7.76 <sup>e</sup> ; 7.738 <sup>k</sup>	7.836 <sup>l</sup> ; 7.846 <sup>m</sup>
Si <sub>1</sub> (8a)	1/8, 1/8, 1/8	1/8, 1/8, 1/8 <sup>ek</sup>	
Si <sub>2</sub> (16d)	1/2, 1/2, 1/2	1/2, 1/2, 1/2 <sup>ek</sup>	
N (32e)	0.2576, 0.2576, 0.2576	( $x, x, x$ ); $x=0.25+\delta$ , $\delta<0.0125$ <sup>e</sup> 0.25968, 0.25968, 0.25968 <sup>k</sup>	$x=0.3843$ <sup>l</sup> ; $x=0.2576$ <sup>m</sup>
$B_0$ (GPa)	304	290 <sup>n</sup>	280 <sup>b</sup> ; 300 <sup>e</sup>

<sup>a</sup>Reference 37.

<sup>b</sup>Reference 26. Orthogonalized linear combination of atomic orbitals (OLCAO).

<sup>c</sup>Reference 29.

<sup>d</sup>Reference 30.

<sup>e</sup>Reference 27.

<sup>f</sup>Reference 40.

<sup>g</sup>Reference 38. Norm-conserving pseudopotential plane wave DFT-LDA.

<sup>h</sup>Reference 39. Hartree-Fock linear combination of atomic orbitals (HF-LCAO).

<sup>i</sup>Reference 31.

<sup>j</sup>Reference 32.

<sup>k</sup>Reference 28.

<sup>l</sup>Reference 41. Orthogonalized linear combination of atomic orbitals (OLCAO).

<sup>m</sup>Reference 42. Gaussian-type basis sets DFT-GGA.

<sup>n</sup>Reference 43.

has the lowest energy followed by (110), and TiN(111) has the highest surface energy.

The interlayer spacings of the N- and Ti-terminated TiN(111) surfaces are shown in Table III. In good agreement with Marlo's results (also shown),<sup>47</sup> the strongest relaxations are found for the N-terminated surface, where the first interlayer spacing contracts by 36%. This is considerably larger than that of the Ti-terminated surface, which contracts by 12%. The second interlayer spacing is significantly expanded (by 23%) for the N-terminated surface, while only slightly expanded (1.8%) for the Ti-terminated surface. For interlayer

spacings further from the surfaces the distance between the layers approaches the bulk value.

### C. Bulk TiSi<sub>2</sub>

Titanium disilicide is also relevant for the present study; as mentioned above, it is the phase from which we determine the silicon chemical potential under N-poor conditions. Titanium disilicide forms a base-centered orthorhombic c49 (Cmcm space group) phase, which has a high resistivity, and a fcc-centered orthorhombic c54 (Fddd space group) phase,

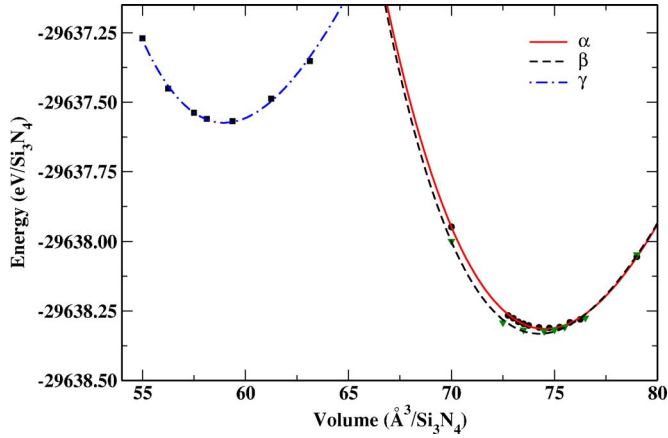


FIG. 2. (Color online) Total energy vs volume for the  $\alpha$ -,  $\beta$ -, and  $\gamma$ - $\text{Si}_3\text{N}_4$  crystal structures.

which has low resistivity.<sup>48</sup> Both structures have six atoms in the unit cell. In determining the total energy for a bulk unit of  $\text{TiSi}_2$ , we fix the  $a/b$  ratio for the c49 phase and the  $a/c$  ratio for the c54 phase and optimize the volume, relaxing all internal parameters. We use a cutoff radius of 9 Bohr, and  $\mathbf{k}$ -point meshes of  $(6 \times 6 \times 4)$  (39  $\mathbf{k}$  points in the IBZ) and  $(4 \times 4 \times 4)$  (18  $\mathbf{k}$  points in the IBZ) for the c49 and c54 phases, respectively. The calculated (experimental) lattice constants for the c49 phase are  $a=3.571 \text{ \AA}$ ,  $b=13.573 \text{ \AA}$ ,  $c=3.556 \text{ \AA}$  ( $a=3.62 \text{ \AA}$ ,  $b=13.76 \text{ \AA}$ ,  $c=3.60 \text{ \AA}$ ). For the c54 phase, the corresponding values are  $a=8.270 \text{ \AA}$ ,  $b=4.801 \text{ \AA}$ ,  $c=8.553 \text{ \AA}$  ( $a=8.269 \text{ \AA}$ ,  $b=4.798 \text{ \AA}$ ,  $c=8.553 \text{ \AA}$ ).

#### IV. INTERFACE STRUCTURE

##### A. Atomic configuration

Before we begin the detailed study of the  $\text{TiN}(111)/\text{Si}_x\text{N}_y/\text{TiN}(111)$  interfaces, we consider the adsorption properties of a single Si atom on the N-terminated  $\text{TiN}(111)$  surface with  $(1 \times 1)$  periodicity in order to check the convergence with respect to the thickness of TiN slab. There are four high-symmetry sites on the  $\text{TiN}(111)$  surface on which Si could bond. As can be seen in Figs. 3(a) and 3(b), Si atoms could occupy the site on top of N atoms or on the bridge site between two N atoms. Also, there are two kinds of hollow sites. The difference between them is related to the Ti atoms in the second layer: in one case, which we

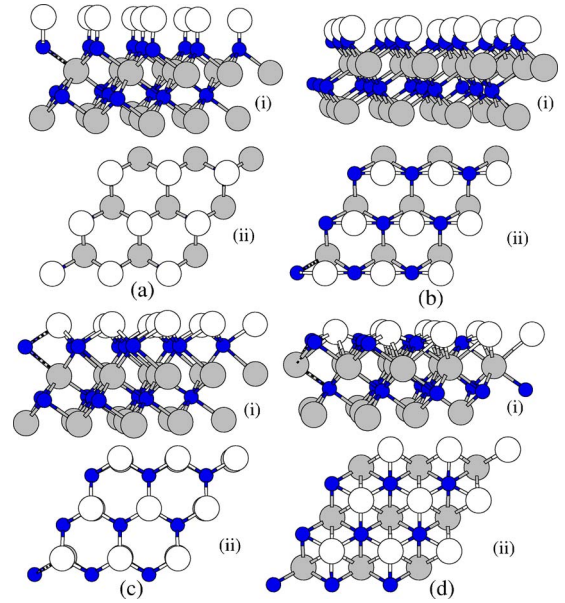


FIG. 3. (Color online) Side (i) and top (ii) view of four high-symmetry adsorption sites for Si on the N-terminated  $(1 \times 1)$ - $\text{TiN}(111)$  surface: (a) the top site, (b) bridge site, (c) hcp-hollow site, (d) fcc-hollow site. Small dark circles represent nitrogen, gray circles Ti, and white circles, Si.

will call the hcp-hollow site, there is a Ti atom in the second layer directly below the Si atom [Fig. 3(c)]. The other hollow site, which we call “fcc-hollow,” is shown in Fig. 3(d). Here there are no Ti atoms in the second layer directly below the Si atoms. The adsorption energy is calculated as  $E_a = \frac{1}{2}(E_{\text{sys}}^{\text{tot}} - E_{\text{TiN}}^{\text{surf}} - 2E_{\text{Si}}^{\text{atom}})$ , where  $E_{\text{sys}}^{\text{tot}}$  and  $E_{\text{TiN}}^{\text{surf}}$  are the total energies of the adsorption system and the clean  $\text{TiN}(111)$  slab, respectively.  $E_{\text{Si}}^{\text{atom}}$  is total energy of a free Si atom. The factors  $\frac{1}{2}$  and 2 arise due to adsorption of Si on both sides of the slab. For these calculations, we use a large  $20 \text{ \AA}$  vacuum region and a  $(6 \times 6 \times 1)$  Monkhorst-Pack grid of special  $\mathbf{k}$  points for integration in reciprocal space, leading to seven  $\mathbf{k}$  points in the surface IBZ. We performed calculations using 7, 9, and 11 TiN layers, with Si atoms in the fcc-hollow site, on each side of the slab. The resulting adsorption energies are  $-4.131$ ,  $-4.2284$ , and  $-4.192 \text{ eV}$ , respectively, implying the calculations are converged to about  $0.037 \text{ eV}$  for nine layers. Using nine TiN layers, calculations for Si in the hcp-hollow site show that this is less favorable compared to the fcc-hollow site by  $0.016 \text{ eV}$ . Adsorption of the Si atom in the

TABLE II. Calculated surface energies,  $\sigma$  (in electron volts per square angstrom), for the relaxed and unrelaxed TiN surfaces. Values in parenthesis are given in electron volts per respective  $(1 \times 1)$  TiN surface unit cell.

Surface	Relaxed			Unrelaxed		
	Present	Ref. 46	Ref. 47	Present	Ref. 46	Ref. 47
(111)	0.214 (2.377)	0.226 (2.510)	0.307 (3.410)	0.309 (3.432)	0.311 (3.455)	0.338 (3.754)
(100)	0.087 (0.789)	0.086 (0.780)	0.080 (0.726)	0.105 (0.952)	0.105 (0.952)	0.109 (0.989)
(110)	0.174 (2.232)	0.177 (2.270)	0.178 (2.283)	0.197 (2.527)	0.197 (2.527)	0.195 (2.501)

bridge site is  $-4.225$  eV, which is only  $0.003$  eV less favorable than the fcc-hollow site. Thus, the adsorption energies of all these three sites are practically degenerate. The most favorable site by far is for Si in the top site where the adsorption energy is  $-4.83$  eV. A Mulliken analysis shows that the Si atom, when in the top site, has a significantly smaller (positive) electron charge density compared to when in the alternative sites, namely,  $0.23$  vs  $\sim 0.5$ – $0.6$ . Correspondingly, the position of the Si- $2p$  level is higher in energy (less negative) by  $>1$  eV as compared to the other sites, reflecting the more negative electronic environment. The Si-N bondlength is also significantly shorter ( $1.76$  Å vs  $2.09$ – $2.05$  Å). Furthermore, the large contraction of the N-terminated TiN(111) surface is significantly reversed for the bridge, hcp-, and fcc-hollow sites and now expands by  $12.8$ ,  $28.0$ , and  $28.5\%$ , respectively, indicating a notably reduced interaction with the Ti atoms below, and hence, the similar adsorption energies. On the other hand for Si in the top site, the first N-Ti layer distance is still notably contracted, namely, by  $11.8\%$ , indicating a greater interaction with the underlying Ti atoms. These features suggest that the Si-N bond for Si in the top site has a smaller ionic and a greater covalent character. This is supported by the partial density of states (PDOS) of the Si atoms and the N atoms to which they bond for the various sites. From Fig. 4, it can be seen that the PDOS look similar for the hollow and bridge (or edge) sites, but there is a greater hybridization of Si  $s$  and  $p$  states with N- $p$  states for the case of Si binding on top of the N atoms.

Based on the convergence checks described above, we choose to use ten layers of TiN(111) in creating the TiN(111)/Si $_x$ N $_y$ /TiN(111) interfaces, i.e., ten-layer-TiN slabs on each side of the Si $_x$ N $_y$  region.

### 1. Simple (1×1) interfaces

We initially consider simple (1×1)-Si interface structures sandwiched between two ten-layer TiN(111) slabs, surrounded by a vacuum region  $20$  Å thick. In these structures, the lateral unit cell distance is  $3.01$  Å. This is  $28\%$  larger than the nearest-neighbor distance in bulk Si, which is  $2.35$  Å. Because of the polar nature of the TiN(111) plane and because we use an even number of layers in the upper and lower TiN slabs, on the interface side of the upper slab there are Ti atoms and on the interface side of the lower slab

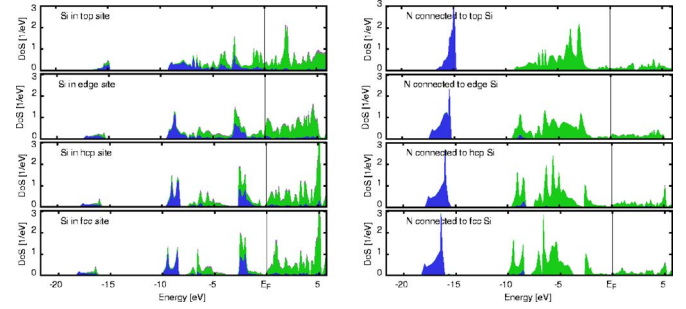


FIG. 4. (Color online) Left: Si atom partial DOS for the various adsorption sites on the N-terminated TiN(111) surface. Right: corresponding results for the N atoms bonded to the Si atoms. The dark gray regions correspond to  $s$  states and the light gray regions  $p$  states.

there are N atoms. We consider three types of simple interfaces consisting of: (i) a pure Si layer, (ii) a SiN layer, and (iii) a TiSi layer. This gives rise to N-Si-Ti, N-Si-N, and Ti-Si-Ti bonding environments, respectively. There are four possible positions for the interface layers relative to the N atoms of the lower slab, namely, top, bridge, hcp-hollow, and fcc-hollow site (cf. Fig. 3). Similarly, there are also four possible sites relative to the Ti-atoms of the upper slab. This gives a total of 16 structures to consider. We label them according to the interface-layers type (Si, SiN, TiSi), and according to the atomic positions of the interface layers relative to the lower and upper slabs. For example, the pure Si layer interface structure containing Si in the top site at the N-terminated lower slab, and the hcp site of the Ti-terminated upper slab, is called “top-hcp-Si.” Similarly, the SiN interface structure containing Si atoms on top of the N atoms of the N-terminated lower slab, and N atoms of the interface layer on the top sites of the Ti-terminated upper slab, is called “top-top-SiN,” and so on. Thus, with these three types of simple interfaces, with 16 possible configurations for each, it amounts to the consideration of 48 different structures. We note that although the pure Si and TiSi layer interface structures are not suggested by experiment (but rather one such that the SiN layer interface yields a N-Si-N environment as indicated by XPS studies<sup>9</sup>), we still consider them theoretically for interest and completeness. It will be shown, in fact, that such structures become favorable under certain conditions.

TABLE III. Calculated interlayer distances,  $d_{ij}$  (in Å), for the N- and Ti-terminated TiN(111) surfaces. Values in parenthesis give the percentage deviation to the bulk interlayer spacing. All values are in angstroms. The experimental value of the interlayer spacing is  $1.224$  Å.

	Ti-terminated Å (%)	Ref. 47 Å (%)	N-terminated Å (%)	Ref. 47 Å (%)
$d_{12}$	1.082 (−12.0)	1.106 (−10.0)	0.787 (−36.0)	0.754 (−39.0)
$d_{23}$	1.252 (1.8)	1.238 (0.7)	1.517 (23.4)	1.555 (26.5)
$d_{34}$	1.248 (1.5)	1.269 (3.0)	1.142 (−7.0)	1.125 (−8.5)
$d_{45}$	1.236 (0.5)	1.282 (4.0)	1.235 (0.4)	1.187 (−3.4)
$d_{56}$	1.221 (−0.7)		1.217 (−1)	
Bulk (theory)	1.230	1.229	1.230	1.229

## 2. Interfaces based on $\text{Si}_3\text{N}_4$

We also consider more complex interface geometries, which are based on the bulk phases of  $\text{Si}_3\text{N}_4$ . In particular, we place one layer of  $(10\bar{1}0)$   $\alpha$ -,  $(10\bar{1}0)$   $\beta$ -, and  $(111)$   $\gamma$ - $\text{Si}_3\text{N}_4$  between the two 10-layer TiN(111) slabs. We call these structures  $\alpha$ -,  $\beta$ - and  $\gamma$ -like interfaces. As before, the interface side of the lower TiN slab is terminated by N atoms and the interface side of the upper TiN slab is terminated by Ti atoms. In each of the  $\alpha$ -,  $\beta$ -, and  $\gamma$ -like interfaces, we keep the nitrogen atoms of the lower N-terminated slab in the regular hexagonal lattice of the TiN(111) plane. These N atoms will be shared by titanium (of the TiN slab) and silicon atoms of the interface. The silicon atoms and nitrogen atoms in the interface layer(s) are strictly distributed in the bulk  $\text{Si}_3\text{N}_4$  positions. The atomic arrangement of the  $\alpha$ -,  $\beta$ - and  $\gamma$ -like interfaces are shown in Figs. 5(a)–5(c), respectively. In each case, image (i) shows a top view of N-terminated TiN(111), i.e., of the lower slab, where the unit cell (parallel to the interface) is indicated; image (ii) shows how the atoms of the respective  $\text{Si}_3\text{N}_4$  layer are arranged in the unit cell with respect to N-terminated TiN(111), and image (iii) shows a side view of the interface system. The lateral unit cell of the  $\alpha$ -like interface corresponds to a  $(2 \times 3)$ -TiN(111) cell, where there are 148 atoms in the system. The  $\beta$ - and  $\gamma$ -like interfaces correspond to  $(1 \times 3)$  and  $(2 \times 2)$ -TiN(111) cells, respectively, where there are 74 and 94 atoms in the system. We keep the lateral lattice constant fixed at that of TiN, which results in a mismatch of the  $\alpha$ -,  $\beta$ -, and  $\gamma$ -like interfaces of 5.9% ( $x$  direction) and 4.9% ( $y$  direction); 2.7% ( $x$  direction) and 5.9% ( $y$  direction); 4.9% ( $x$  direction) and 8.3% ( $y$  direction), respectively. For all cases, the lateral TiN(111) cells are larger than the corresponding ideal  $\text{Si}_3\text{N}_4$  cells, i.e., the  $\alpha$ -,  $\beta$ -, and  $\gamma$ -like interfaces are under tensile strain compared to the corresponding bulk  $\alpha$ -,  $\beta$ -, and  $\gamma$ - $\text{Si}_3\text{N}_4$ -like structures. The thickness of the  $\alpha$ -,  $\beta$ -, and  $\gamma$ - $\text{Si}_3\text{N}_4$ -like interfaces shown in Fig. 5 is about 6.72, 6.50, and 4.52 Å, respectively. We recall that the experimentally reported thickness, as mentioned in the Introduction, is 3–5 Å.

In addition to these  $\text{Si}_3\text{N}_4$ -based interfaces, which contain a complete  $\text{Si}_3\text{N}_4$  layer, we also consider thinner  $\text{Si}_3\text{N}_4$  derived layers. Specifically, for the  $\beta$ -like interface, the center N-layer [indicated by c in Fig. 5(b)] could replace either of the N-layers labeled a or d giving rise to  $\beta$ -like  $\text{Si}_2\text{N}_3$  and  $\beta$ -like  $\text{Si}_4\text{N}_5$  films of 2.24 and 4.26 Å thickness, respectively. We do not consider the interface resulting where the N-layer labeled b replaces either a or d, since the N-atoms in this layer are not distributed hexagonally and hence would yield a bonding quite different to in either bulk TiN or  $\text{Si}_3\text{N}_4$ , which we expect to be unfavorable. For the  $\gamma$ -like interface, the center N-layer [see Fig. 5(c), label b] could be shared with the Ti atoms, i.e., could replace either of the N-layers labeled a or c, to yield two  $\gamma$ -like  $\text{Si}_3\text{N}_4$  films of 2.09 and 2.43 Å, respectively. Since the Si atoms in  $\gamma$ -like  $\text{Si}_3\text{N}_4$  films with 2.09 Å are sixfold coordinated to the surrounding N atoms, we call it “ $\gamma$ -like  $\text{Si}_3\text{N}_4(6)$ ,” and the Si atoms in the 2.43 Å films are fourfold coordinated to the surrounding N atoms; this is thus labeled “ $\gamma$ -like  $\text{Si}_3\text{N}_4(4)$ .” For the  $\alpha$ -like

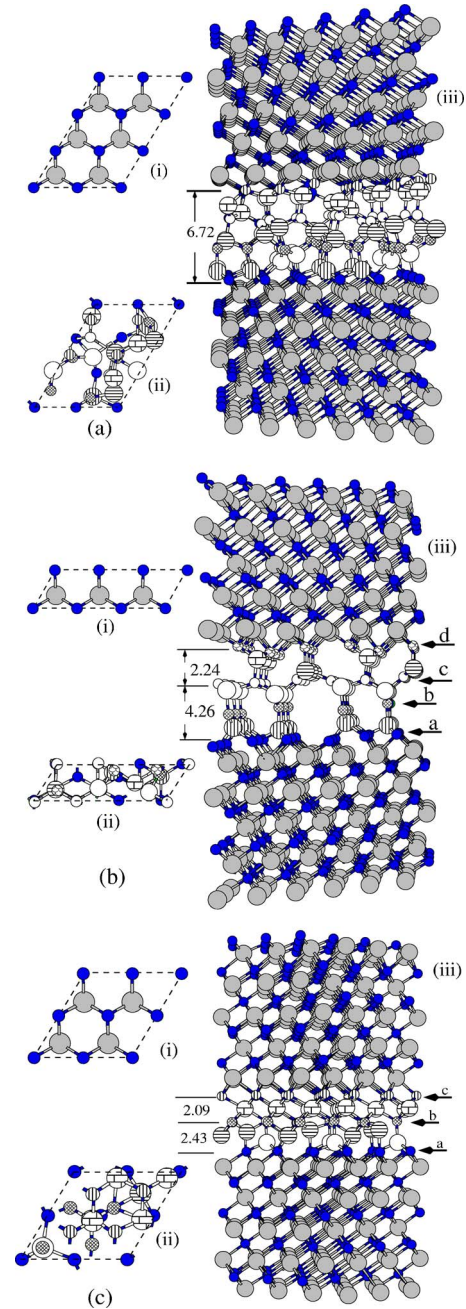


FIG. 5. (Color online) Atomic structures of the  $\text{Si}_3\text{N}_4$ -like interface structures. (i) Top view of the N-terminated TiN(111) (lower) slab showing the unit cell of the interface system, (ii) top view showing the relative positions of the atoms of the (a)  $(2 \times 3)$   $\alpha$ - $\text{Si}_3\text{N}_4(10\bar{1}0)$ , (b)  $(1 \times 3)$   $\beta$ - $\text{Si}_3\text{N}_4(10\bar{1}0)$ , and (c)  $(2 \times 2)$   $\gamma$ - $\text{Si}_3\text{N}_4(111)$  layers, relative to the N atoms of the N-terminated TiN(111) (lower) slab, (iii) side view of the  $\alpha$ -,  $\beta$ -, and  $\gamma$ -like interfaces. Nitrogen, silicon, and titanium atoms are indicated by small, large white (or hatched), and large gray circles, respectively.

interface, only a complete (periodic)  $\alpha$ - $\text{Si}_3\text{N}_4(10\bar{1}0)$  layer will yield an interface where all Ti, N, and Si atoms are coordinated to their neighbors as in bulk TiN and  $\alpha$ - $\text{Si}_3\text{N}_4$ , thus we do not consider thinner  $\alpha$ -like structures as we expect they will be less favorable.

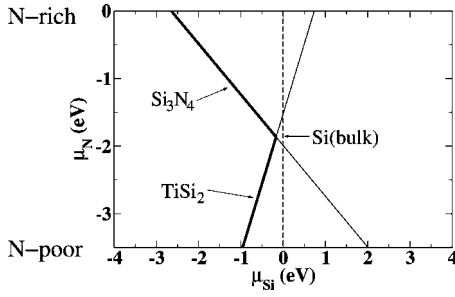


FIG. 6. The silicon chemical potential  $\mu_{\text{Si}}$  vs the nitrogen chemical potential,  $\mu_{\text{N}}$ , as obtained from bulk silicon (dashed line), from (c49)  $\text{TiSi}_2$  and  $\beta\text{-Si}_3\text{N}_4$  as labeled. The nitrogen chemical potential is given with respect to half the total energy of the  $\text{N}_2$  molecule, and the silicon chemical potential is given with respect to the total energy of a Si atom in bulk.

### B. Interfacial formation energy

Before discussing the resulting interface formation energies, we explain, in more detail, our choice of the silicon chemical potential,  $\mu_{\text{Si}}$ . In order to have a realistic estimate of the formation energy, we must determine  $\mu_{\text{Si}}$  from the most stable phase for a given value of the nitrogen (or corresponding titanium) chemical potential. From Fig. 6 it can be seen that for N-rich conditions ( $\mu_{\text{N}} = 1/2E_{\text{N}_2}$ ) the lowest energy  $\mu_{\text{Si}}$  is obtained from bulk  $\beta\text{-Si}_3\text{N}_4$ . For increasingly less N-rich conditions,  $\mu_{\text{Si}}$  as determined this way decreases and at  $\mu_{\text{N}} = -1.87$  eV,  $\mu_{\text{Si}}$  obtained from bulk (c49)  $\text{TiSi}_2$  is equivalent. For increasingly more N-poor conditions (more negative values of  $\mu_{\text{N}}$ ),  $\mu_{\text{Si}}$  is lowest when obtain from bulk  $\text{TiSi}_2$ . For all values of the nitrogen chemical potential,  $\mu_{\text{Si}}$  as obtained from bulk silicon, is never the lowest energy. Thus, in evaluating the formation energies as a function of  $\mu_{\text{N}}$ , we use the values of  $\mu_{\text{Si}}$  indicated by the bold lines in Fig. 6.

Selected interface formation energies are listed in Table IV, and the formation energies of all 55 considered structures (except those that lie off the scale) are plotted in Fig. 7 as a function of the nitrogen chemical potential. It can be seen from Fig. 7 that the  $\beta$ -derived  $(1 \times 3)\text{-Si}_2\text{N}_3$  configuration [see Fig. 8(b)] is the energetically most favorable for nitrogen-rich conditions. Interestingly, in this fully relaxed structure, both the Si and Ti atoms are tetrahedrally coordi-

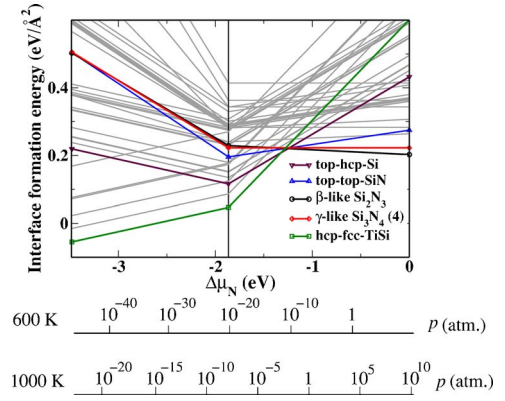


FIG. 7. (Color online) Interface formation energies as a function of the nitrogen chemical potential  $\mu_{\text{N}}$  for all considered configurations. The lowest energy structures are labeled. The nitrogen chemical potential has been correlated with the pressure for two selected temperatures of 600 and 1000 K [cf. Eq. 6].

nated, while in bulk  $\text{TiN}$ , the Ti atoms bonds to six N atoms, i.e., are octahedrally coordinated. The  $\gamma$ -like  $\text{Si}_3\text{N}_4(4)$  structure shown in Fig. 8(c) should also be mentioned since it is the second most stable configuration for N-rich conditions. It is interesting to note that both these configurations contain only tetrahedrally N-coordinated Si and Ti atoms at the interface. This may be related to the fact that both the  $\alpha$ - and  $\beta\text{-Si}_3\text{N}_4$  phases, where the Si atoms are tetrahedrally N coordinated, are more stable than the  $\gamma\text{-Si}_3\text{N}_4$  phase, which also contains some Si atoms that are sixfold (octahedrally) N coordinated. The reason then that the  $\gamma$ -like  $\text{Si}_3\text{N}_4(4)$  interface (with only tetrahedrally N-coordinated Si) is less favorable may be related to the larger lattice mismatch as compared to the  $\beta$ -like  $\text{Si}_2\text{N}_3$  structure, as described earlier.

For more N-poor conditions, Fig. 7 shows that the  $(1 \times 1)$  top-hcp-Si interface structure [Fig. 8(d)] becomes most stable, but only for a very small range of the nitrogen chemical potential, i.e.,  $\mu_{\text{N}} = -1.25$  to  $-1.32$  eV. For  $\mu_{\text{N}} < -1.32$  eV, the Ti-Si-Ti bonded interface [ $(1 \times 1)$  hcp-fcc-TiN] is favorable. This structure is illustrated in Fig. 8(e). The interface structure displayed in Fig. 8(a) [ $(1 \times 1)$  top-top-SiN] involving a N-Si-N bonding configuration is also low in energy for a value of the nitrogen chemical potential around  $-1.25$  eV, where all five interface structures are practically degenerate.

TABLE IV. Selected formation energies. Values are in electron volts per square angstrom and in brackets, electron volts per  $(1 \times 1)\text{-TiN}(111)$  unit cell. The lowest energies are indicated in bold type.

Configurations	$E^f$ for N-poor	$E^f$ for $\mu_{\text{N}} = -1.87$ eV	$E^f$ for N-rich
top-top-SiN	0.504 (5.598)	0.196 (2.177)	0.274 (3.044)
top-hcp-Si	0.219 (2.433)	0.116 (1.288)	0.432 (4.799)
hcp-fcc-TiSi	<b>-0.055 (-0.611)</b>	<b>0.047 (0.522)</b>	0.601 (6.677)
$\alpha$ -like $\text{Si}_3\text{N}_4$	1.168 (12.974)	0.414 (4.599)	0.414 (4.599)
$\beta$ -like $\text{Si}_3\text{N}_4$	1.117 (12.407)	0.363 (4.032)	0.363 (4.032)
$\gamma$ -like $\text{Si}_3\text{N}_4$	0.909 (10.097)	0.344 (3.821)	0.344 (3.821)
$\beta$ -like $\text{Si}_2\text{N}_3$	0.503 (5.587)	0.229 (2.544)	<b>0.202 (2.244)</b>
$\gamma$ -like $\text{Si}_3\text{N}_4(4)$	0.505 (5.609)	0.222 (2.466)	0.222 (2.466)

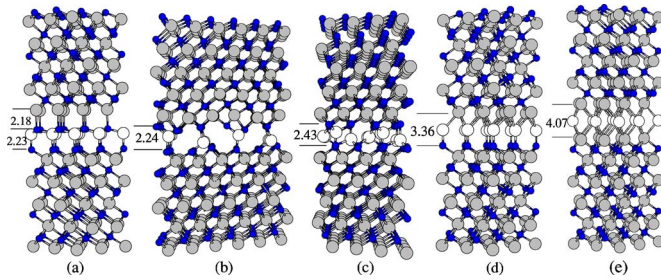


FIG. 8. (Color online) The interfaces which have the lowest formation energies: (a)  $(1 \times 1)$  top-top-SiN, (b)  $\beta$ -like  $(1 \times 3)$ - $\text{Si}_2\text{N}_3$ , (c)  $\gamma$ -like  $(2 \times 2)$ - $\text{Si}_3\text{N}_4$ , (d)  $(1 \times 1)$  top-hcp-Si, and (e)  $(1 \times 1)$  hcp-fcc-TiSi. Small dark, large gray, and white circles represent N, Ti, and Si atoms, respectively. Selected interlayer distances are given in angstroms.

It is informative to correlate the N-chemical potential to its dependence on the  $\text{N}_2$  gas pressure and temperature through the expression,

$$\mu_{\text{N}}(T, p_{\text{N}_2}) = \frac{1}{2} \left[ E_{\text{N}_2}^{\text{total}} + \tilde{\mu}_{\text{N}}(T, p^0) + k_{\text{B}} T \ln \left( \frac{p_{\text{N}_2}}{p^0} \right) \right], \quad (4)$$

as obtained by manipulation of the ideal gas equations.<sup>49</sup> Here  $p_{\text{N}_2}$  is the nitrogen pressure,  $p^0$  corresponds to atmospheric pressure, and  $k_{\text{B}}$  is the Boltzmann constant. The temperature dependence of  $\tilde{\mu}_{\text{N}}(T, p^0)$  in the standard state (1 atm), which describes the contribution from rotations and vibrations of the molecule, is taken from the tabulated thermodynamic data.<sup>50</sup> In Fig. 7, the resulting pressure variation for the range of the nitrogen chemical potential for two selected temperatures is given. With this, we can then consider the experimental conditions under which the nanocomposites are created and see which interface structure has the lowest predicted energy. Before doing so, we first consider the magnitude of vibrational and entropic contributions to the free energies of formation. We do this for the most favorable  $\beta$ -like  $\text{Si}_2\text{N}_3$ -interface. We require the vibrational frequencies,  $\omega_i$ , for this interface and the reference, 20-layer TiN(111) slab. This is obtained by constructing and diagonalizing the dynamical matrix, and then using

$$E_{\text{vib}}(T, \omega) = \frac{1}{(2\pi)^3} \sum_i \frac{1}{2} \hbar \omega_i + k_{\text{B}} T \ln \left[ 1 - \exp \left( -\frac{\hbar \omega_i}{k_{\text{B}} T} \right) \right], \quad (5)$$

where  $k_{\text{B}}$  is the Boltzmann constant. The contribution is plotted in Fig. 9 where to compare to the interface formation energy in electron volts per square angstrom, the energy is divided by the corresponding interface area. It can be seen for temperatures right up to 1000 K, the value is very small and thus will not affect the relative stability of the various interface structures.

In the studies of Meng *et al.*,<sup>51</sup> a hardness enhancement was not found for the *nc*-TiN/*a*- $\text{Si}_3\text{N}_4$  nanocomposites, in contrast to the results of Veprek and Reiprich<sup>5</sup> and Veprek *et al.*<sup>13</sup> Here, the measured hardness was found to be  $< 32$  GPa and to vary smoothly with the Si composition, rather than

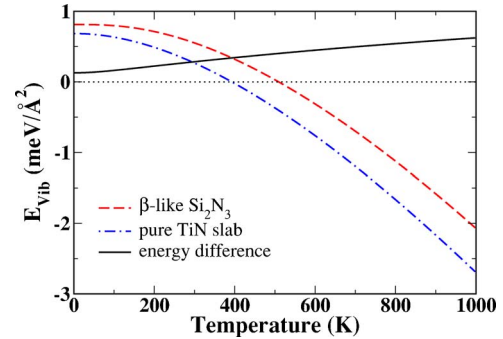


FIG. 9. (Color online) Vibrational contribution to the free energy of interface formation (full curve), and the contributions from the reference TiN(111) slab (dot-dashed curve) and the  $\beta$ -like  $\text{Si}_2\text{N}_3$ -interface (dashed curve).

exhibiting a peak for a very thin Si layer (3–4 Å). These experiments employed Ar and  $\text{N}_2$  gas input flows fixed at 10/1.1 with the total pressure kept at  $\sim 1.8$  mTorr during all depositions. This implies a  $\text{N}_2$  partial pressure of 0.178 mTorr (or  $2.34 \times 10^{-7}$  atm.). The measured substrate temperature was approximately 250 °C (523 K). From Fig. 7, it can be seen that at this pressure and temperature, the lowest energy interface is the  $\beta$ -like  $\text{Si}_2\text{N}_3$  structure. The transition to the hcp-fcc-TiSi structure occurs at about  $10^{-10}$  atm at 600 K; at the slightly lower temperature of 523 K, the  $\text{N}_2$  gas pressure at which this transition is predicted to occur will be even smaller. In comparison, the experiments of Veprek *et al.*,<sup>13</sup> reporting the hardness enhancement, employ notably higher temperatures (i.e.,  $> 500$  °C or 773 K) and an  $\text{N}_2$  pressure of the order of 0.1 mbar (around  $10^{-4}$  atm.). From Fig. 7, these conditions would also predict the lowest energy interface is the  $\beta$ -like  $\text{Si}_2\text{N}_3$  structure, but the corresponding N-chemical potential lies closer to that at which the transition to the Ti-Si-N (and Ti-Si-Ti) interfaces are more stable. This suggests that on purely *thermodynamic* considerations, the same structures should be achievable under the respective experimental conditions. Kinetic limitations, however, for atomic rearrangements, may actually prevent the realization of the lowest energy interface structure being realized for the study of Meng *et al.*<sup>51</sup> carried out at 250 °C (523 K). In this respect, from a study on the spinodal nature of the phase segregation, and formation of stable nanostructures, in the Ti-Si-N system, Zhang and Veprek<sup>52</sup> conclude that “kinetic constraints, such as deposition temperatures of less than 300 °C and low nitrogen pressures (although within the range where the stoichiometric TiN and  $\text{Si}_3\text{N}_4$  structures should be fully spinodal), will kinetically hinder the system to reach the thermodynamically driven equilibrium.” Thus, the conflicting results described above, could be due to the formation of different interface structures. Alternatively, the difference could have another cause, namely, oxygen contamination, as suggested recently in Refs. 13 and 14. Figure 7 also shows that at high temperatures (e.g., 600–700 °C or 873–973 K) and low nitrogen pressures (e.g.,  $< 10^{-4}$  or  $10^{-5}$  atm) interfaces involving Ti-Si-Ti bonding at the interface become favorable.

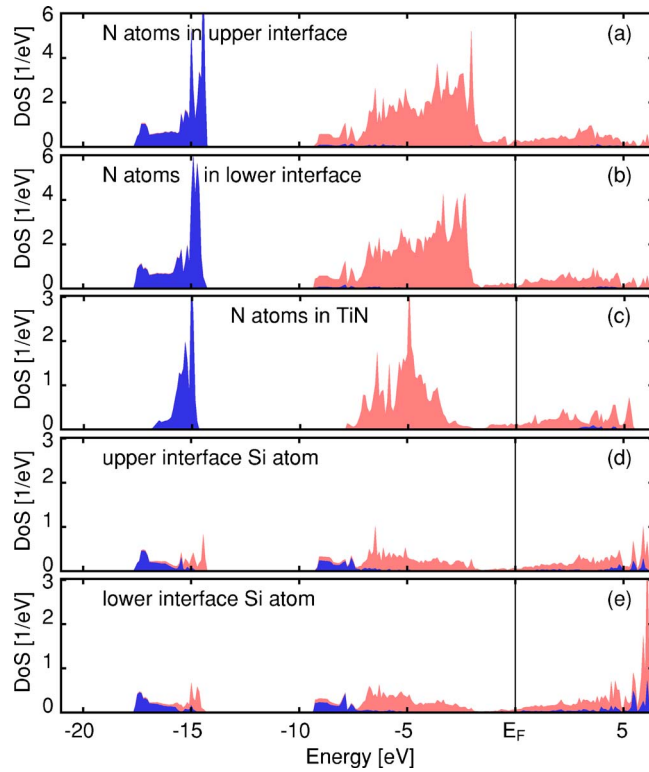


FIG. 10. (Color online) Atom partial DOS of various atoms (as labeled) of the favorable  $(1 \times 3)$ -TiN(111)/ $\beta$ -Si<sub>2</sub>N<sub>3</sub>/TiN(111) interface [Fig. 8(b)]. The dark gray regions correspond to *s*-states and the light gray regions *p*-states.

### C. Electronic structure

The PDOS for the N atoms and Si atoms of the  $\beta$ -like Si<sub>2</sub>N<sub>3</sub> interface [Fig. 8(b)] are shown in Fig. 10. In contrast to the PDOS for bulk  $\beta$ -Si<sub>3</sub>N<sub>4</sub> (Fig. 11), which show that the material is insulating with a band gap of about 4 eV, the interface system is metallic with Si and N *p* states at the Fermi level. This is due to Si-3*p*-N-2*p* hybridization, where

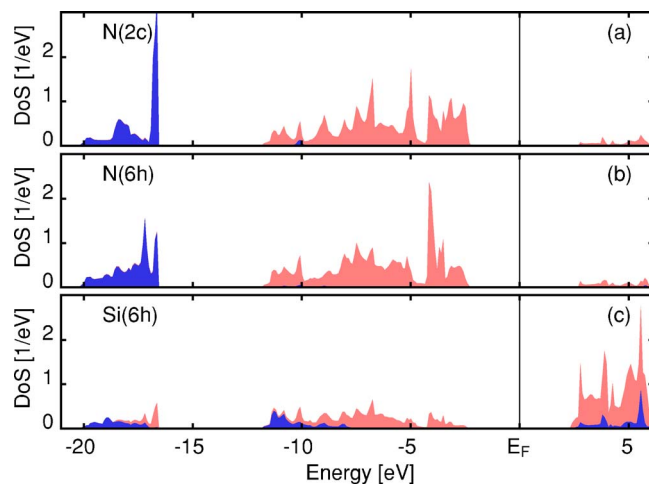


FIG. 11. (Color online) Partial DOS for the N and Si atoms of  $\beta$ -Si<sub>3</sub>N<sub>4</sub>. The dark gray regions correspond to *s*-states and the light gray regions *p*-states.

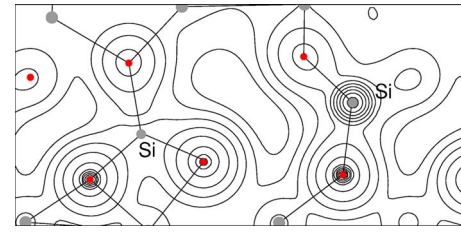


FIG. 12. (Color online) Electron charge density of the  $\beta$ -like  $(1 \times 3)$ -Si<sub>2</sub>N<sub>3</sub> interface. The first contour line is at  $0.01 e \text{ Bohr}^{-3}$  with a spacing of  $2.154 e \text{ Bohr}^{-3}$ . The cross-section plane passes through the center of the Si-N bond in the right of the plot, and through the lower N atom to the left of the plot.

the N atoms are also hybridized with the Ti atoms, which have a significant 3*d* PDOS at the Fermi level.<sup>45</sup> In Fig. 12, a cross section of the valence electron density is shown where the two tetrahedrally coordinated Si atoms can be seen.

We recall that it was proposed that the local Si bonding geometry in the *nc*-TiN/*a*-Si<sub>3</sub>N<sub>4</sub> was similar to that in bulk  $\beta$ -Si<sub>3</sub>N<sub>4</sub> on the basis that the Si-2*p* core level was at a similar energy in each system. It is therefore interesting to compare the calculated Si-2*p* position of the various low-energy interface structures with that determined for bulk  $\beta$ -Si<sub>3</sub>N<sub>4</sub>. We obtain the following relative differences: For the energetically favorable  $\beta$ -like Si<sub>2</sub>N<sub>3</sub> interface system, the Si-2*p* state is 1.1 eV higher (less negative) in energy; for the top-*top*-SiN interface system, which also involves tetrahedrally N-bonded Si, it is 0.4 eV higher in energy; for the  $\gamma$ -like Si<sub>3</sub>N<sub>4</sub> interface, the value is 1.4 eV higher in energy; and for the top-hcp-Si interface system (involving N-Si-Ti bonding), the deviation becomes larger, namely, 1.8 eV higher in energy; and for the interface structure hcp-fcc-TiSi (which involves Ti-Si-Ti bonding) and is predicted most favorable for N-poor conditions, the deviation becomes larger still, i.e., 2.3 eV. Thus, we have the trend that the more Si-Ti bonds involved, the greater the deviation to the Si-2*p* state in bulk  $\beta$ -Si<sub>3</sub>N<sub>4</sub> (as would be expected). Coming back to the experimental results, the bulk Si<sub>3</sub>N<sub>4</sub> Si-2*p* state is at  $-102.2$  eV (Ref. 54) while in the nanocomposites it is  $-101.7$ , i.e., 0.6 eV higher in energy. This deviation is closest to those found theoretically for the structures involving only N-coordinated Si, as described above. This shift to higher energy is consistent with the Si atom of the interface region being in a more negative electronic environment compared to in bulk  $\beta$ -Si<sub>3</sub>N<sub>4</sub>. The experimental value of the Si-2*p* state in TiSi<sub>2</sub> is at  $-99.3$  eV,<sup>55</sup> a deviation of 2.4 eV as compared to bulk  $\beta$ -Si<sub>3</sub>N<sub>4</sub>. This relative deviation is very similar to that found for the Si atom of the hcp-fcc-TiSi interface as mentioned above, with a difference of 2.3 eV.

Considering the  $\beta$ -like Si<sub>2</sub>N<sub>3</sub> interface favored under nitrogen-rich conditions, the single N-Si bond of Si to the lower N-terminated slab is shorter (1.706 and 1.715 Å) as compared to the average distance in bulk  $\beta$ -Si<sub>3</sub>N<sub>4</sub> (1.74 Å). This suggests a stronger N-Si bond, which is found to be the case from calculation of the work of separation<sup>53</sup> for breaking the single Si-N bonds in the  $\beta$ -like Si<sub>2</sub>N<sub>3</sub>. Namely, it is larger than for the corresponding bonds of the (10 $\bar{1}$ 0) ori-

ented bulk  $\beta$ - $\text{Si}_3\text{N}_4$  system ( $0.219 \text{ eV}/\text{\AA}^2$  vs  $0.199 \text{ eV}/\text{\AA}^2$ ). This may be a factor contributing to the observed hardness enhancement in the nanocomposites.

## V. CONCLUSION

We performed extensive first-principles DFT calculations using DMol<sup>3</sup> in order to help shed light on the atomic structure and associated physical properties of superhard  $nc$ -TiN/ $a$ - $\text{Si}_3\text{N}_4$  nanocomposites. For the three  $\alpha$ ,  $\beta$ , and  $\gamma$  phases of bulk  $\text{Si}_3\text{N}_4$ , we calculated the optimized atomic structure, bulk modulus, and heat of formation, which are in excellent agreement with available experimental results. With the aim of elucidating the atomic structure of the TiN(111)/ $\text{Si}_x\text{N}_y$ /TiN(111) interfaces, we considered 55 possible configurations. For nitrogen-rich conditions a so-called  $\beta$ -like ( $1 \times 3$ )  $\text{Si}_2\text{N}_3$  structure involving tetrahedral N-Si-N bonding is most favorable, while for nitrogen-poor conditions a ( $1 \times 1$ )-TiSi structure is preferred involving octahedral Ti-Si-Ti bonding. For the interface structure predicted under nitrogen-rich conditions (involving tetrahedrally purely N-coordinated Si), the work of separation of such interfaces is slightly greater than for the corresponding value from bulk  $\beta$ - $\text{Si}_3\text{N}_4$ . This, together with the specific crystallographic orientation of interface may be factors contributing

to the observed hardness enhancement in the nanocomposites.

By correlating the nitrogen chemical potential with the pressure and temperature of  $\text{N}_2$  gas, considering only thermodynamics, it appears that most experiments are performed under conditions where the  $\beta$ -like  $\text{Si}_2\text{N}_3$  interface is predicted to be favorable, but still could be close to where the transition from to the hcp-fcc-TiSi interface structure occurs. Kinetic hindering effects for the experimental systems will clearly play an important role if too low temperatures are employed and may prevent the formation of the structure predicted purely on thermodynamic grounds. Some of the deviations in the reported hardnesses of the N-Si-Ti films could be attributed to this, in that the atomic structure of the interface may be different, and not that which is thermodynamically most stable. Another possibility is that oxygen impurities play a role, and we will investigate this in a forthcoming publication.

## ACKNOWLEDGMENTS

We thank Stan Veprek for stimulating discussions. We are grateful for the computing resources provided by the Australian Partnership for Advanced Computing (APAC) National Facility and the Australian Center for Advanced Computing and Communications (AC3). This work was supported by the Australian Research Council (ARC).

\*Corresponding author. Electronic address: stampfl@physics.usyd.edu.au

<sup>1</sup>H. F. George and H. K. John, Phys. Rev. **93**, 1004 (1954).

<sup>2</sup>L. E. Toth, *Transition Metal Carbides and Nitrides* (Academic Press, New York, 1971).

<sup>3</sup>F. de Brito Mota, J. F. Justo, and A. Fazzio, Phys. Rev. B **58**, 8323 (1998).

<sup>4</sup>T. P. Ma, IEEE Trans. Electron Devices **45**, 680 (1998).

<sup>5</sup>S. Veprek and S. Reiprich, Thin Solid Films **268**, 64 (1995).

<sup>6</sup>R. A. Andrievski, Int. J. Refract. Met. Hard Mater. **19**, 447 (2001).

<sup>7</sup>V. V. Brazhkin and A. G. Lyapin, Philos. Mag. A **82**, 231 (2002).

<sup>8</sup>P. Karvankova, M. Veprek-Heijman, O. Zindulka, A. Bergmaier, and S. Veprek, Surf. Coat. Technol. **163-164**, 149 (2003).

<sup>9</sup>S. Veprek, A. Niederhofer, K. Moto, T. Bolom, H.-D. Männling, P. Nesladek, G. Dollinger, and A. Bergmaier, Surf. Coat. Technol. **133-134**, 152 (2000).

<sup>10</sup>S. Veprek, J. Vac. Sci. Technol. **17**, 2401 (1999).

<sup>11</sup>S. Veprek, P. Karvankova, J. Prochazka, and H. Männling, MRS Fall Meeting, Boston Symposium P, 2001.

<sup>12</sup>W. J. Meng, X. D. Zhang, B. Shi, R. C. Tittsworth, L. E. Rehn, and P. M. Baldo, J. Mater. Res. **17**, 2628 (2002).

<sup>13</sup>S. Veprek, H. D. Mannling, A. Niederhofer, D. Ma, and S. Mukherjee, J. Vac. Sci. Technol. **22**, 1071 (2004).

<sup>14</sup>S. Veprek, P. Karvankova, and M. G. J. Veprek-Heijman (to be published).

<sup>15</sup>H. Söderberg, J. M. Molina-Aldareguia, L. Hultman, and M. Odén, J. Appl. Phys. (to be published).

<sup>16</sup>Y.-H. Chen, K. W. Lee, W.-A. Chiou, Y.-W. Chung, and L. M.

Keer, Surf. Coat. Technol. **146**, 209 (2001).

<sup>17</sup>X. Hu, H. Zhang, J. Dai, G. Li, and M. Gu, J. Vac. Sci. Technol. **23**, 114 (2005).

<sup>18</sup>C. Iwamoto and S. Tanaka, J. Am. Ceram. Soc. **81**, 363 (1998).

<sup>19</sup>B. Delley, J. Chem. Phys. **92**, 508 (1990).

<sup>20</sup>B. Delley, J. Chem. Phys. **113**, 7756 (2000).

<sup>21</sup>J. P. Perdew, K. Burke, and M. Ernzerhof, Phys. Rev. Lett. **77**, 3865 (1996).

<sup>22</sup>F. D. Murnaghan, Proc. Natl. Acad. Sci. U.S.A. **50**, 697 (1944).

<sup>23</sup>P. Goodman and M. O'Keeffe, Acta Crystallogr., Sect. B: Struct. Crystallogr. Cryst. Chem. **36**, 2891 (1980).

<sup>24</sup>R. Grun, Acta Crystallogr., Sect. B: Struct. Crystallogr. Cryst. Chem. **35**, 800 (1979).

<sup>25</sup>R. Belkada, M. Kohyama, T. Shibayanagi, and M. Naka, Phys. Rev. B **65**, 92104 (2002).

<sup>26</sup>W. Y. Ching, L. Ouyang, and J. D. Gale, Phys. Rev. B **61**, 8696 (2000).

<sup>27</sup>A. Zerr, G. Miehe, G. Serghiou, M. Schwarz, E. Kroke, R. Riedel, H. Fuess, P. Kroll, and R. Boehler, Nature (London) **400**, 340 (1999).

<sup>28</sup>M. Schwarz, G. Mehe, A. Zerr, E. Kroke, B. T. Poe, and H. Fuess, Adv. Mater. (Weinheim, Ger.) **12**, 883 (2000).

<sup>29</sup>M. B. Kruger, J. H. Nguyen, Y. M. Li, W. A. Caldwell, M. H. Manghnani, and R. Jeanloz, Phys. Rev. B **55**, 3456 (1997).

<sup>30</sup>O. Yeheskel and Y. Gefen, Mater. Sci. Eng. **71**, 95 (1985).

<sup>31</sup>L. Cartz and J. D. Jorgensen, J. Appl. Phys. **52**, 236 (1981).

<sup>32</sup>Y. M. Li, M. B. Kruger, J. H. Nguyen, W. A. Caldwell, and R. Jeanloz, Solid State Commun. **103**, 107 (1997).

<sup>33</sup>H. J. Monkhorst and J. D. Pack, Phys. Rev. B **13**, 5188 (1976).

- <sup>34</sup> *Handbook of Chemistry and Physics*, edited by R. C. Weast, M. J. Astle, and W. H. Beyer (Chemical Rubber Co., Boca Raton, 1988), Vol. 69.
- <sup>35</sup> P. A. G. O'Hare, *Pure Appl. Chem.* **71**, 1243 (1999).
- <sup>36</sup> L. V. Gurvich, I. V. Veyts, and C. B. Alcock, *Thermodynamic Properties of Individual Substances* (Hemisphere Publishing, New York, 1991, Vol. 2).
- <sup>37</sup> H. F. Priest, F. C. Burns, G. L. Priest, and E. C. Skaar, *J. Am. Ceram. Soc.* **56**, 395 (1973).
- <sup>38</sup> R. Belkada, T. Shibayanagi, M. Naka, and M. Kohyama, *J. Am. Ceram. Soc.* **83**, 2449 (2000).
- <sup>39</sup> A. Reyes-Serrato, D. H. Galvan, and I. L. Garzon, *Phys. Rev. B* **52**, 6293 (1995).
- <sup>40</sup> O. Borgen and H. M. Seip, *Acta Chem. Scand.* (1947-1973) **15**, 1789 (1961).
- <sup>41</sup> S.-D. Mo, L. Ouyang, W. Y. Ching, I. Tanaka, Y. Koyama, and R. Riedel, *Phys. Rev. Lett.* **83**, 5046 (1999).
- <sup>42</sup> P. Mori-Sanchez, M. Marqués, A. Beltrán, J. Z. Jiang, L. Gerward, and J. M. Recio, *Phys. Rev. B* **68**, 64115 (2003).
- <sup>43</sup> A. Zerr, M. Kempf, M. Schwarz, E. Kroke, M. Göken, and R. Riedel, *J. Am. Ceram. Soc.* **85**, 86 (2002).
- <sup>44</sup> A. N. Christiansen, *Acta Chem. Scand., Ser. A* **32**, 87 (1978).
- <sup>45</sup> C. Stampfl, W. Mannstadt, R. Asahi, and A. J. Freeman, *Phys. Rev. B* **63**, 155106 (2001).
- <sup>46</sup> S. V. Dudiy and B. I. Lundqvist, *Phys. Rev. B* **69**, 125421 (2004).
- <sup>47</sup> M. Marlo and V. Milman, *Phys. Rev. B* **62**, 2899 (2000).
- <sup>48</sup> R. Rosenkranz and G. Frommeyer, *Z. Metallkd.* **83**, 9 (1992).
- <sup>49</sup> K. Reuter and M. Scheffler, *Phys. Rev. B* **65**, 035406 (2002).
- <sup>50</sup> D. R. Stull and H. Prophet, *JANAF Thermochemical Tables*, 2nd ed. (U.S. National Bureau of Standards, Washington, DC, 1971).
- <sup>51</sup> W. J. Meng, X. D. Zhang, B. Shi, R. C. Tittsworth, L. E. Rehn, and P. M. Baldo, *J. Mater. Res.* **17**, 2628 (2002).
- <sup>52</sup> R. F. Zhang and S. Veprek (unpublished).
- <sup>53</sup> The work of separation is calculated as  $E_w = E_{\text{tot}}^{12} - E_{\text{tot}}^1 - E_{\text{tot}}^2$  where  $E_{\text{tot}}^{12}$ ,  $E_{\text{tot}}^1$ ,  $E_{\text{tot}}^2$  are the total energies of the interface system containing parts 1 and 2, and the total energy of the separated parts 1 and 2 of the system, respectively, which are sufficiently far enough apart so as not to interact.
- <sup>54</sup> K. D. Vargheese and G. M. Rao, *J. Vac. Sci. Technol.* **19**, 2122 (2001).
- <sup>55</sup> S. M. Lee, E. T. Ada, H. Lee, J. Kulik, and J. W. Rabalais, *Surf. Sci.* **453**, 159 (2000).